Nanoengineering Ni_xFe_{1-x} Catalysts for Gas-Phase, Selective Synthesis of Semiconducting Single-Walled Carbon Nanotubes

Wei-Hung Chiang,[†] Mohammed Sakr,[‡] Xuan P. A. Gao,[§,*] and R. Mohan Sankaran[†,*]

[†]Department of Chemical Engineering, Case Western Reserve University, Cleveland, Ohio 44106, [‡]Department of Physics, Faculty of Science, Alexandria University, Egypt, and [§]Department of Physics, Case Western Reserve University, Cleveland, Ohio 44106

ABSTRACT The inhomogeneity of as-grown single-walled carbon nanotubes (SWCNTs), in terms of chiral structure, is a major obstacle to integration of these novel materials in advanced electronics. While separation methods have circumvented this problem, current synthesis approaches must be refined for large-scale production of SWCNTs with uniform properties. In addition, it is highly desirable to alter the initial chirality distribution which constrains fundamental study and applications. Here, we demonstrate that semiconducting SWCNTs are selectively produced in the gas phase by engineering catalysts at the nanoscale with precise size and composition. The semiconducting content in as-grown mixtures of SWCNTs is assessed by UV—visible—NIR absorbance and micro-Raman spectroscopy and reaches a maximum purity of 90% for samples catalyzed by $Ni_{0.27}Fe_{0.73}$ nanoparticles (2.0 nm mean diameter). Electrical studies are performed on thin film transistors (TFTs) fabricated from as-grown SWCNTs and reveal high on/off current ratios of 10^3.

KEYWORDS: bimetallic · nanoparticle · carbon nanotube · chirality

Single-walled carbon nanotubes (SWCNTs) have received a great deal of interest for a number of electronic applications because of their novel properties including high on−off current ratio,[1] high electron/hole mobilities,[2] ability to support high current densities,[3] and stability at high frequencies.[4] Many of these applications require nanotubes of a single electronic type, which is determined by their chiral structure.[5,6] Current growth methods produce mixtures of metallic and semiconducting chiralities that create significant problems for direct integration in electronics.[7] Considerable research efforts have been spent addressing this issue and succeeded in purifying or separating SWCNTs by electronic type after growth *via* electrophoresis,[8] physiochemical modification,[9] density gradient ultracentrifugation (DGU),[10] electrical breakdown,[11] and gas-phase plasma etching.[12] While postgrowth separation of SWCNT mixtures has made high-purity semiconducting or metallic nanotubes available for fundamental study,[1,10,13] these schemes remain unsuitable for commercial applications because they are time-consuming, expensive, difficult to scale up, and may introduce defects or even damage the nanotubes.[7] In addition, separation methods are constrained by the distribution and concentration of various chiralities in the initial mixture. For this reason, there is a critical need to refine the growth process to improve the homogeneity of as-grown SWCNTs and selectively grow specific nanotube structures.

Several methods have been developed for the selective growth of SWCNTs.[14−18] Among these, the floating catalyst method where metal nanoparticles are prepared in the gas phase is the most attractive for large-scale synthesis of SWCNTs.[19−21] The chirality distribution of as-grown SWCNTs produced by the floating catalyst method has been altered by exploring different catalyst materials, such as a supported mixture of CoMo, which has been found to produce narrow distributions of smaller diameter nanotubes.[22] This result is supported by theoretical studies which suggest that the catalyst plays a crucial role during nanotube nucleation and growth and may determine the final nanotube structure.[23,24] We have recently shown that careful tuning of the catalyst composition is a potential route to controlling the chirality distribution of SWCNTs.[25] The catalyst shape has also been modified to obtain higher fractions of nanotubes of a specific electronic type.[26] Here, we demonstrate that the catalyst composition, independent of other parameters, influences the semiconducting SWCNT (s-SWCNT) content in as-grown nanotubes. Detailed optical characterization by

*Address correspondence to xuan.gao@case.edu, mohan@case.edu.

Received for review September 14, 2009 and accepted November 19, 2009.

Published online December 2, 2009. 10.1021/nn901222t

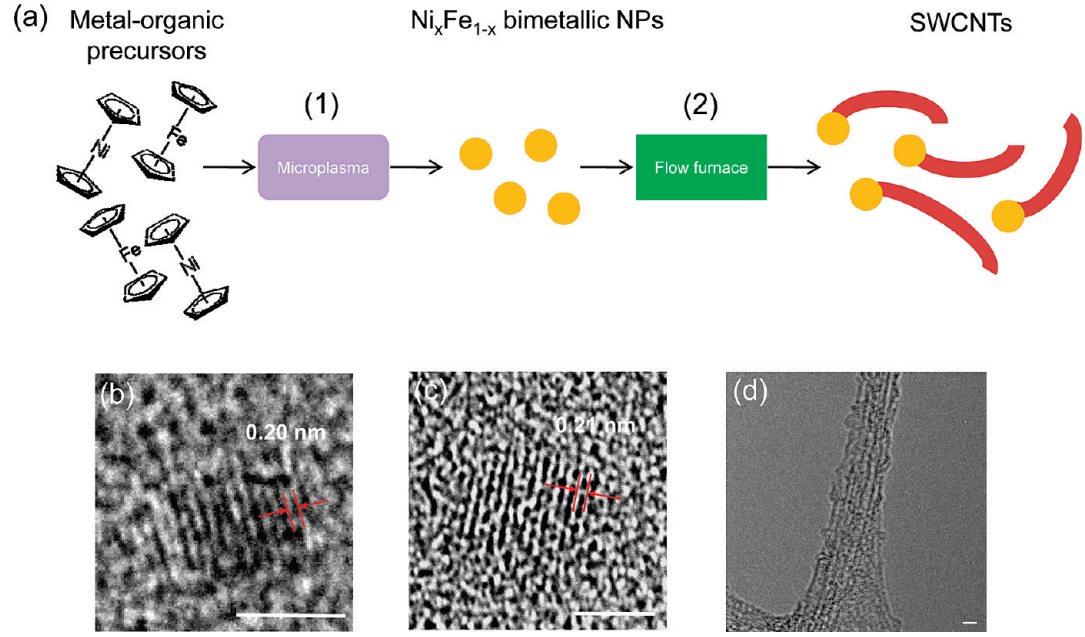

Figure 1. (a) Stepwise, gas-phase process for SWCNT growth consisting of (1) microplasma synthesis of compositionally tuned bimetallic nanoparticles and (2) thermal growth of carbon nanotubes. Representative HRTEM images of (b) Ni and (c) $Ni_{0.27}Fe_{0.73}$ nanoparticles grown in a microplasma reactor at 2.0 ppm nickelocene and 1.3 ppm total metallocene vapor concentration (27:73 nickelocene/ferrocene) in Ar, respectively (scale bar = 2 nm). (d) Representative HRTEM image of Ni-catalyzed SWCNTs grown at 600 °C (scale bar = 2 nm).

UV−visible−NIR absorbance and micro-Raman spectroscopy reveals that SWCNTs grown with $Ni_{0.27}Fe_{0.73}$ nanocatalysts, as compared to other catalyst compositions, are highly enriched in semiconducting nanotubes with a purity of more than 90%. Thin film devices fabricated from as-grown SWCNTs are found to exhibit on−off ratios as high as 10^3, confirming that $Ni_{0.27}Fe_{0.73}$ nanocatalysts preferentially grow s-SWCNTs.

RESULTS AND DISCUSSION

Figure 1a illustrates the stepwise, gas-phase process used to grow SWCNTs. Details of the process have been previously reported.[27−29] Briefly, metal-organic precursors (*i.e.*, nickelocene and ferrocene) are dissociated in a microplasma to form mono- or bimetallic nanoparticles of precise size and composition. Careful control of the process parameters is required to tune the particle composition independent of its size. For this study, we prepared a series of Ni_xFe_{1-x} nanoparticles with varying composition from $x = 1.0$ to 0 (x = atomic fraction) and constant mean diameter of 2.0 nm. The standard deviations of the particle size distributions were determined by aerosol measurements to be less than 15% (Supporting Information, Figure S1). We separately collected and performed *ex situ* microcharacterization of the nanocatalysts. High-resolution transmission electron microscopy (HRTEM) analysis reveals that Ni nanoparticles exiting the microplasma are spherical and crystalline. A representative particle in Figure 1b exhibits a lattice spacing of 0.20 nm, which corresponds to the (111) plane of face-centered cubic (fcc) Ni. In comparison, the HRTEM image of a representative $Ni_{0.27}Fe_{0.73}$ nanoparticle shows a slightly increased lattice spacing for the (111) plane of 0.21 nm (Figure 1c). TEM images were used to independently obtain the size and distribution of Ni and $Ni_{0.27}Fe_{0.73}$ nanoparticles and show excellent correspondence with aerosol measurements (Supporting Information, Figure S2). We attribute the slightly larger mean diameter observed in TEM to surface oxidation of the particles during transfer into the instrument. To evaluate the composition of *individual* Ni_xFe_{1-x} nanoparticles, we employed energy-dispersive spectroscopy (EDX) (Supporting Information, Figure S3). The relative ratio of the spectral peak intensities for the Ni Kα and Fe Kα lines was used to establish a compositional variation between different $Ni_{0.27}Fe_{0.73}$ nanoparticles of less than 6%. The crystal structure of the nanoparticles was determined by X-ray diffraction (XRD) (Supporting Information, Table S1). Thin films of Ni nanoparticles were found to exhibit fcc crystalline phase, consistent with TEM observations. As Fe is incorporated into the nanoparticles, there is an expansion of the fcc structure, as indicated by the larger lattice parameter. The corresponding increase in the bond length of the (111) plane supports TEM observations. When the Fe concentration is more than 50%, as in the case of $Ni_{0.27}Fe_{0.73}$ nanoparticles, XRD shows the coexistence of fcc and bcc crystalline phases. The structural analysis is largely consistent with the thermodynamic phase diagram of bulk NiFe alloys.[30,31]

To grow SWCNTs, the as-grown nanocatalysts were directly introduced into a heated flow furnace and exposed to controlled mixtures of hydrogen and acetylene. The furnace reactor was operated at the same gas

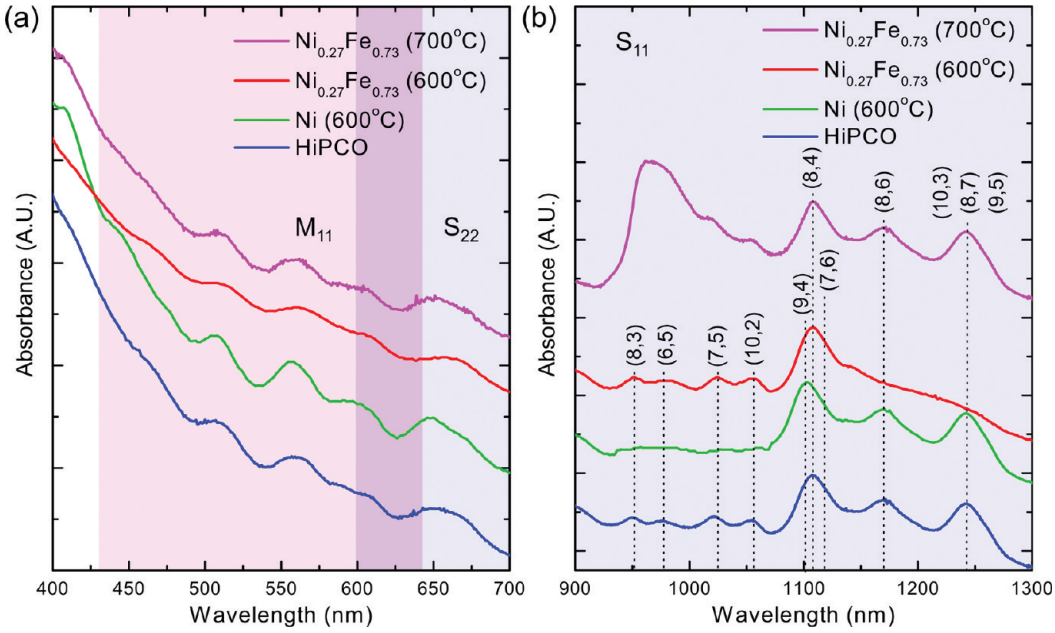

Figure 2. (a,b) UV−visible−NIR absorbance spectra of SDS-dispersed SWCNTs grown with compositionally tuned Ni_xFe_{1-x} nanocatalysts (2.0 nm mean particle diameter) at indicated furnace temperatures. The absorbance spectrum of a HiPCO sample is also included for comparison. The absorbance spectra are offset for clarity. The labels S_{11} and S_{22} (shaded blue) indicate the excitonic optical absorption bands for semiconducting SWCNTs corresponding to the first and second one-dimensional van Hove singularities, respectively, and the M_{11} (shaded pink) label corresponds to the first-order transition of metallic SWCNTs.[32]

concentration and residence time to maintain identical growth conditions, except for the catalyst composition and furnace temperature. The collected product was initially characterized by HRTEM, which confirmed the presence of high purity SWCNTs in the as-grown reactor product (Figure 1d). The nanotubes were collected, dispersed, and diluted as necessary to obtain identical absorbance intensities at 587 nm; these concentration-adjusted samples were then used for optical characterization. The overall yield of SWCNTs in terms of concentration was found to be similar in all samples, but longer nanotubes are expected at higher reactor temperatures due to the higher growth rates.[29] While individual SWCNTs were separated from bundled and larger diameter tubes during dispersion, we emphasize that the tubes were not chemically purified or separated on the basis of chirality in order to ensure that the properties of as-grown SWCNTs were directly related to the catalyst.

We initially performed UV−visible−NIR absorbance to estimate the metallic and semiconducting content in various SWCNT samples. Figure 2 shows UV−visible−NIR absorbance spectra, offset for illustration (no normalization), collected from SDS/D_2O-dispersed solutions of SWCNTs grown with Ni and $Ni_{0.27}Fe_{0.73}$ nanocatalysts. An absorbance spectrum of purified SWCNTs made by the commercial HiPCO process (90% purity, Carbon Nanotechnologies Inc., Houston, Texas) is also included for comparison. The labels S_{11} (830−1100 nm) and S_{22} (600−800 nm) indicate the excitonic optical absorption bands for s-SWCNTs corresponding to the first and second one-dimensional van Hove singularities, respectively, and the M_{11} (440−645 nm) label corresponds to the absorption band of metallic SWCNTs (m-SWCNTs).[32] For SWCNTs grown with Ni nanocatalysts at 600 °C, the peak envelopes corresponding to intrinsic excitations of the S_{11}, S_{22}, and M_{11} transitions are clearly observed in the spectra, similar to the HiPCO product, reflecting a mixture of semiconducting and metallic nanotubes (Figure 2a,b). In comparison, the spectrum for $Ni_{0.27}Fe_{0.73}$-catalyzed SWCNTs at 600 °C shows peaks in the S_{11} region without significant contribution from the M_{11} and S_{22} bands (Figure 2a,b), suggesting a narrow chirality distribution enriched in smaller diameter s-SWCNTs. At higher growth temperatures, the $Ni_{0.27}Fe_{0.73}$-catalyzed SWCNTs are found to contain a broader chirality distribution, as inferred by the re-emergence of peaks in the M_{11} and S_{22} region of the absorbance spectrum. Detailed evaluation of the absorbance results is summarized in the Supporting Information, Table S2. Assuming that the peak intensity at 587 nm is proportional to the overall concentration of nanotubes, the absorbance results suggest that, at low temperature (~600 °C), $Ni_{0.27}Fe_{0.73}$ nanocatalysts produce a higher purity of semiconducting nanotubes than Ni.

To further assess the semiconducting and metallic content in our SWCNT samples, micro-Raman spectroscopy with multiple excitation wavelengths was employed. Spectra were normalized with respect to the tangential graphite band (G-band) intensity, which corresponds to the C−C stretching mode at ~1590 cm^{-1}

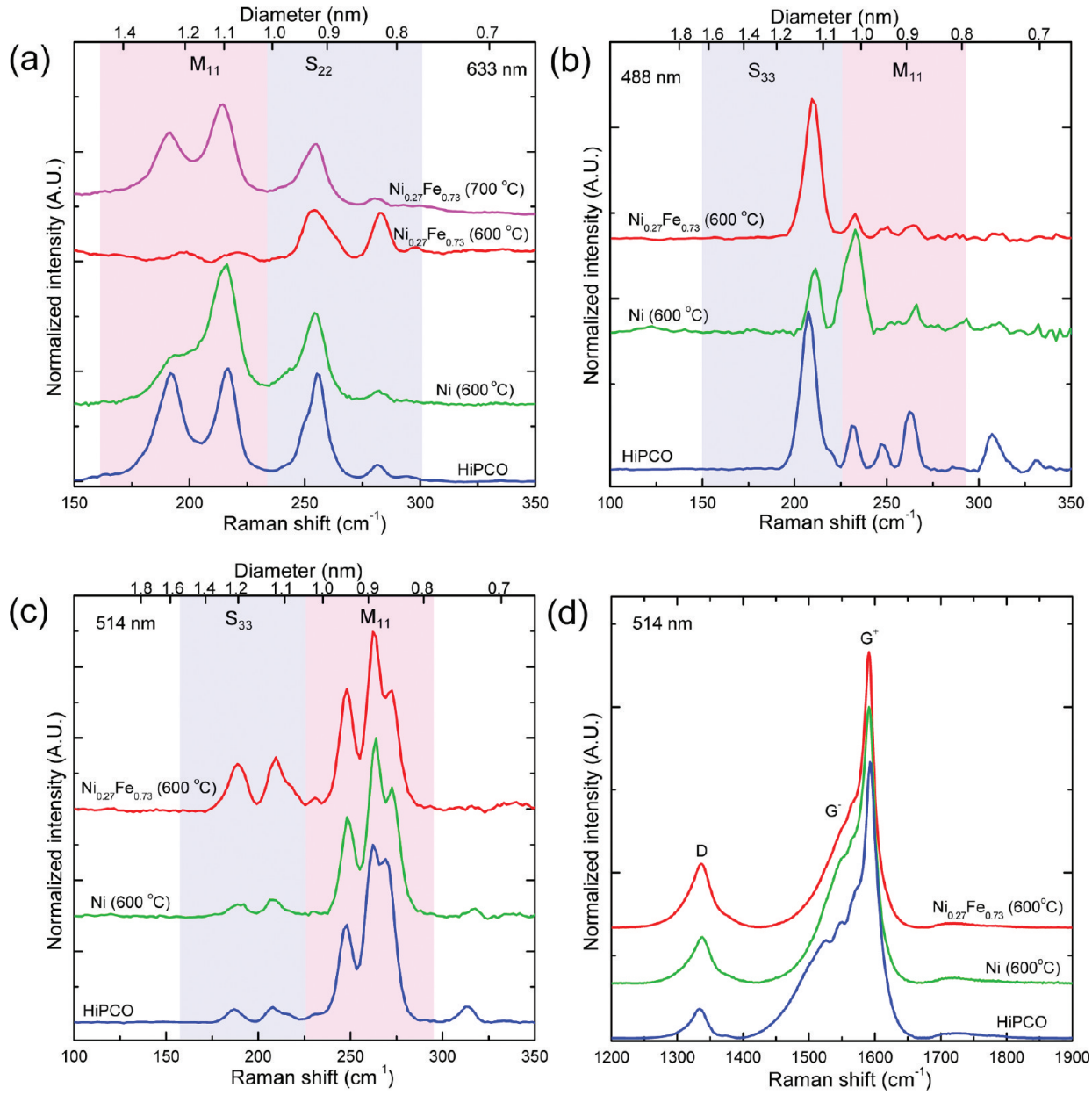

Figure 3. Radial breathing mode (RBM) regions of micro-Raman spectra at (a) 633, (b) 488, and (c) 514 nm excitation wavelengths collected from SWCNTs samples grown with compositionally tuned Ni_xFe_{1-x} nanocatalysts (2.0 mean particle diameter) at indicated furnace temperatures. The spectral regions corresponding to the second- and third-order semiconducting transitions are labeled S_{22} and S_{33} (shaded blue), respectively, and the first-order metallic transition is labeled M_{11} (shaded pink). (d) High frequency region of micro-Raman spectra at 514 nm excitation for SWCNT samples grown with compositionally tuned Ni_xFe_{1-x} nanocatalysts (2.0 mean particle diameter). The Raman spectra of a HiPCO sample at the same excitation wavelengths are included for comparison.

(ωG^+).[33] Raman spectra also exhibit radial breathing mode (RBM) peaks in the range of 120−350 cm^{-1}, characteristic of SWCNTs, and disorder band (D-band) at 1310 cm^{-1} (ref 33). The ratio of the D- to G-band intensity in each spectrum confirms that all samples consist primarily of SWCNTs (Supporting Information, Figure S4), which is consistent with HRTEM analysis. In the RBM region, the frequencies, ω_{RBM} (cm^{-1}), can be related to the nanotube diameter, d_t, by a correlation of the form $\omega_{RBM} = A/d_t + B$, where A and B are empirical parameters. Because of the similarity of our experimental system and sample preparation to that reported by Bachilo *et al.*,[34] we have used the HiPCO product as a reference for Raman analysis (Supporting Information, Table S3). Figure 3a−c shows the RBM regions of the Raman spectra at three different excitations with chirality assignments based on a Kataura plot.[35] We first performed RBM analysis at 633 nm excitation. Compared to the HiPCO product, our SWCNTs grown at 600 °C with Ni nanocatalysts are similar, with only a slight decrease for the Raman peak intensity associated with a metallic nanotube structure at 195 cm^{-1} (Figure 3a). For SWCNTs catalyzed by $Ni_{0.27}Fe_{0.73}$ at 600 °C, the semiconducting peaks at 254 and 283 cm^{-1} are much stronger

TABLE 1. Summary of Micro-Raman Analysis for Ni- and $Ni_{0.27}Fe_{0.73}$-Catalyzed SWCNT Samples (Commercial HiPCO Was Used as the Reference with Recently Reported Values for the Semiconducting and Metallic Content)[36]

excitation wavelength (nm)	temperature (°C)	catalyst	% semiconducting	% metallic	fwhm of G-band intensity (cm^{-1})
633		HiPCO	62.9	37.1	–
	600	Ni	66.8	33.2	–
	600	$Ni_{0.27}Fe_{0.73}$	90.5	9.5	–
	700	$Ni_{0.27}Fe_{0.73}$	55.5	44.5	–
488		HiPCO	62.9	37.1	–
	600	Ni	63.4	36.6	–
	600	$Ni_{0.27}Fe_{0.73}$	85.5	14.5	–
514		HiPCO	62.9	37.1	40
	600	Ni	60.2	39.8	39
	600	$Ni_{0.27}Fe_{0.73}$	84.2	15.8	25

in intensity and the metallic peaks virtually disappear from the spectrum. Moreover, the diameter analysis suggests a shift to a smaller diameter distribution for $Ni_{0.27}Fe_{0.73}$-catalyzed SWCNTs. As the growth temperature is increased, the metallic peaks grow in intensity and the diameter distribution appears to broaden.

RBM analysis at 488 and 514 nm excitation (Figure 3b,c) similarly shows stronger semiconducting peaks at 209 and 233 cm^{-1} and 188 and 209 cm^{-1}, respectively, for nanotubes catalyzed at 600 °C by $Ni_{0.27}Fe_{0.73}$ as compared to Ni. While metallic peaks are observed at 514 nm excitation in the $Ni_{0.27}Fe_{0.73}$-catalyzed sample, the overall metallic content is inferred to be less than the Ni-catalyzed or HiPCO samples. This is further reinforced by the corresponding G-bands at 514 nm excitation for the Ni-catalyzed and HiPCO samples, which are characterized by a broad Breit−Wigner−Fano (BWF) line shape, indicating strong metallic contribution (Figure 2d).[1,14] We find that the full width at half-maximum (fwhm) of the G-band is 1.6 times as large for SWCNTs catalyzed by Ni as compared to $Ni_{0.27}Fe_{0.73}$ (Table 1).

The 633 nm excitation is resonant with metallic and semiconducting nanotubes in a nearly 50:50 ratio and has been extensively used to estimate the s-SWCNT content of an unknown sample by analyzing ratios of integrated Raman RBM intensities and comparing to a HiPCO standard.[1] In view of the recently reported ratio of 37.1%:62.9% metallic-to-semiconducting SWCNTs for the HiPCO product,[36] we estimate a semiconducting content of 90.5% in our $Ni_{0.27}Fe_{0.73}$-catalyzed sample grown at 600 °C[14,37] (Table 1). Similar calculations at the 488 and 514 nm excitations also indicate more than 80% s-SWCNTs in the $Ni_{0.27}Fe_{0.73}$-catalyzed sample (Table 1). In comparison, samples grown with Ni nanocatalysts at the same temperature and $Ni_{0.27}Fe_{0.73}$ nanocatalysts at higher temperatures are found to contain significantly higher fractions of metallic nanotubes. Overall, the micro-Raman analysis is in accordance with absorbance results and confirms preferential growth of s-SWCNTs with $Ni_{0.27}Fe_{0.73}$ nanocatalysts at 600 °C.

To corroborate the micro-Raman analysis, we carried out electrical measurements on the as-grown SWCNT samples. Figure 4a shows a schematic diagram of a SWCNT-based thin film transistor (TFT) with a back-gate, top-contact geometry that was used in this study. Our fabrication methodology allows multiple devices to be obtained in a single step, as shown in Figure 4b. The thin films consist of a network of SWCNTs covering the area between the electrodes (Figure 4b). The average length of the nanotubes is approximately 300 nm, significantly shorter than the channel length of 2 μm. Following thin film preparation, we used micro-Raman spectroscopy to obtain two-dimensional maps and verify the presence and chiralities of SWCNTs. The false

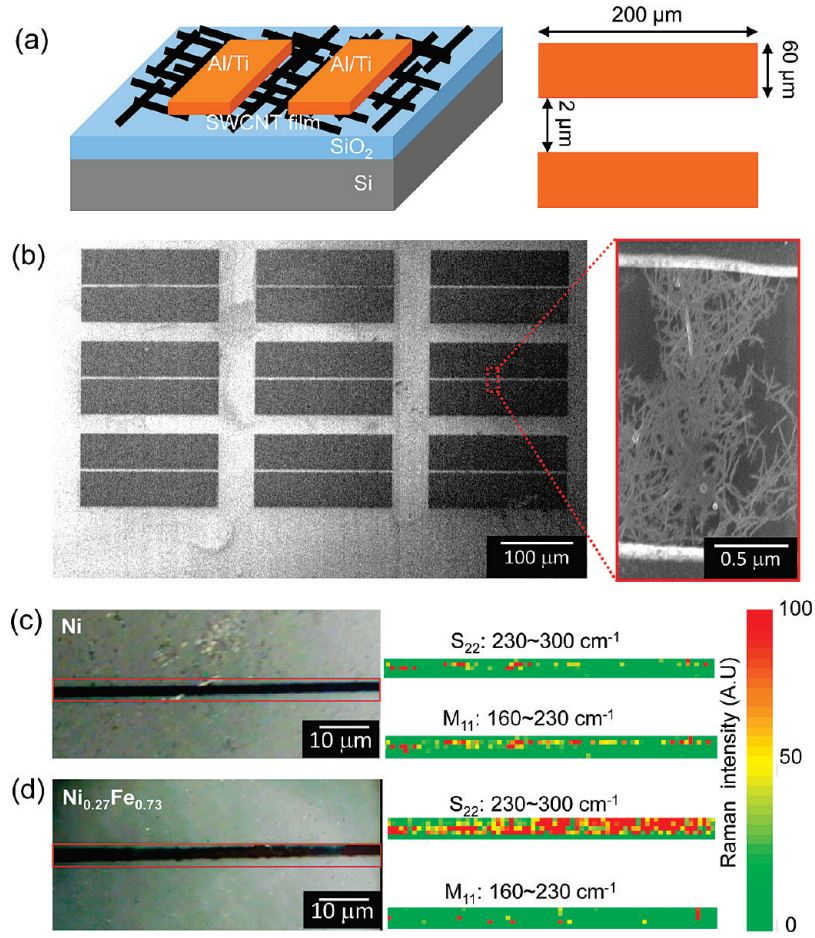

Figure 4. (a) Schematic diagram of SWCNT-based thin film transistor (TFT). (b) SEM images of devices fabricated with SWCNT samples. Charge-coupled detector images and corresponding Raman intensity maps of devices fabricated with (c) Ni- and (d) $Ni_{0.27}Fe_{0.73}$-catalyzed SWCNTs, respectively. The false color maps are proportional to the integrated intensity of the Raman bands ranging from 160 to 230 and 230 to 300 cm^{-1} for semiconducting and metallic nanotubes, respectively.

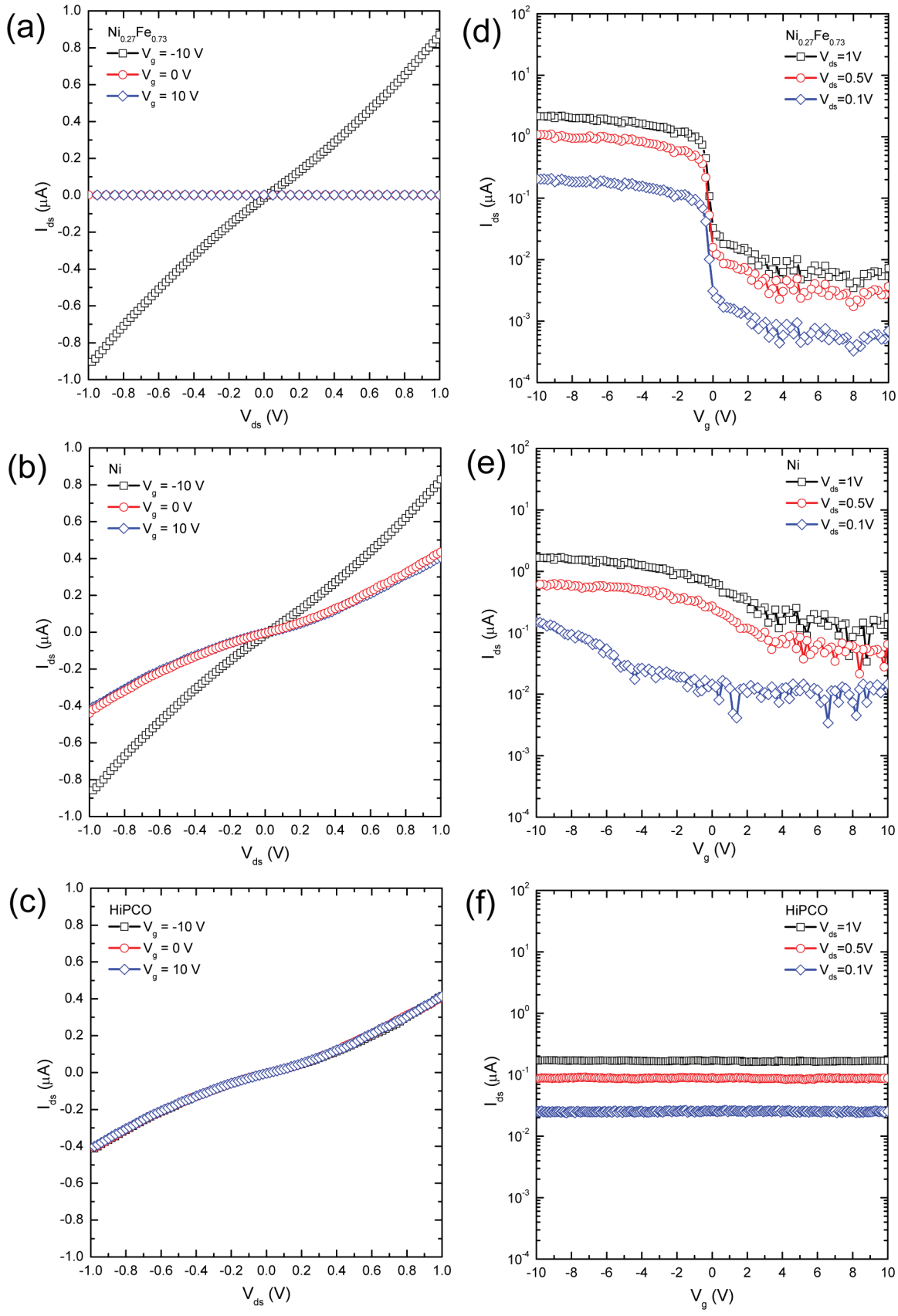

Figure 5. Current−voltage characteristics (I_{ds}−V_{ds} curves) of thin film transistors fabricated with (a) $Ni_{0.27}Fe_{0.73}$ -catalyzed SWCNTs, (b) Ni-catalyzed, and (c) HiPCO sample at different gate voltages (V_g) from −10 to 10 V in steps of 10 V. Transfer characteristics (I_{ds}−V_g curves) of devices fabricated with (d) $Ni_{0.27}Fe_{0.73}$- and (e) Ni-catalyzed SWCNTs, and (f) HiPCO sample at different bias voltages (V_{ds}) of 1, 0.5, and 0.1 V.

color maps were generated by scanning a 633 nm laser beam over an area of 5 × 200 μm² in 1 μm steps and integrating the RBM bands from 230 to 300 cm^{-1} for semiconducting tubes or 160 to 230 cm^{-1} for metallic tubes.[35] Figure 4c,d shows excellent correspondence between the chirality distribution of nanotubes in the devices and the corresponding starting material (compare to Figure 3). Devices fabricated with $Ni_{0.27}Fe_{0.73}$-catalyzed nanotubes exhibit higher intensities for the semiconducting peaks detected at 633 nm excitation than those made from Ni-catalyzed nanotubes.

We fabricated 81 devices on a single substrate for each SWCNT sample to perform a statistically large number of electrical studies. Our process yielded 25, 22, and 30 working devices for $Ni_{0.27}Fe_{0.73}$-catalyzed nanotubes, Ni-catalyzed nanotubes, and the HiPCO sample, respectively. Output characteristics of representative devices fabricated from the three SWCNT samples are shown in Figure 5a−c as a function of gate voltage, V_g. At each gate voltage, the drain voltage (V_{ds}) was swept from 1 to −1 V in steps of −0.05 V. The characteristics of the device containing $Ni_{0.27}Fe_{0.73}$-catalyzed SWCNTs at 600 °C clearly resemble a field-effect transistor (FET), where the source−drain current (I_{ds}) increases with higher negative gate bias. In contrast, devices fabricated from Ni-catalyzed SWCNTs at 600 °C and the HiPCO product show virtually no field-effect behavior. Figure 5d−f shows corresponding logarithmic plots of the I_{ds} *versus* V_g at different V_{ds} for the different devices. At each V_{ds}, the V_g is swept from 10 to −10 V in steps of −0.2 V. The drain current for the device composed of $Ni_{0.27}Fe_{0.73}$-catalyzed SWCNTs at 600 °C increases with decreasing gate voltage, indicative of typical p-type semiconductor behavior (Figure 5d). The strong field-effect behavior of this SWCNT-based device is explained by the high semiconducting content, whereas virtually no field-effect behavior is observed for devices made from Ni-catalyzed nanotubes at 600 °C or HiPCO samples because of the high metallic content. At V_{ds} = 1 V, we estimate an I_{on}/I_{off} ratio of more than 100 for the device fabricated with $Ni_{0.27}Fe_{0.73}$-catalyzed SWCNTs. This is comparable to SWCNT-based FETs grown by plasma-enhanced CVD (PECVD), where the semiconducting fraction was estimated to be more than 96%.[14] Figure 6 shows a histogram of I_{on}/I_{off} ratios obtained for all the FETs fabricated and tested with the various SWCNT samples. More than 50% of the devices composed of $Ni_{0.27}Fe_{0.73}$-catalyzed SWCNTs are found to exhibit an I_{on}/I_{off} ratio of greater than 100. To estimate the semiconducting fraction, we can divide the channel into seven smaller sections, equivalent to the average length of the nanotubes (7 × 300 nm ∼ 2 μm). Since the sections are electrically connected in series, in order for the device to exhibit a high on/off ratio, only a single section must contain all semiconducting nanotubes. From the SEM image, we find that each section

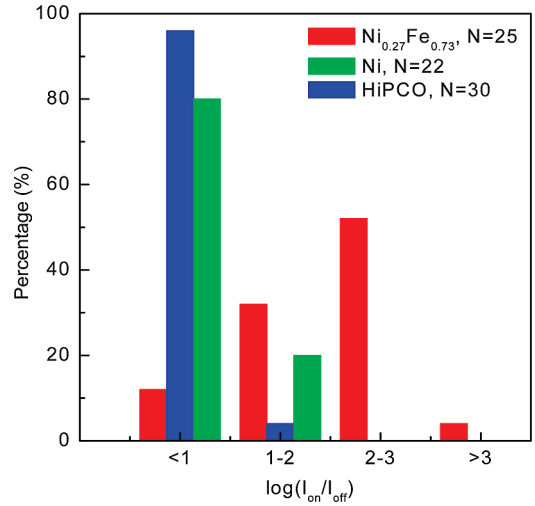

Figure 6. Histograms of on/off current (I_{on}/I_{off}) obtained for devices fabricated with indicated SWCNT samples. *N* is the number of devices tested.

contains approximately 15 nanotubes. Thus, we approximate the fraction of semiconducting nanotubes in the $Ni_{0.27}Fe_{0.73}$-catalyzed sample to be 84% based on a simple probability analysis ($7 \times 0.84^{15} = 0.50$).[13] Overall, the electrical studies confirm a high fraction of s-SWCNTs in the as-grown $Ni_{0.27}Fe_{0.73}$-catalyzed sample, which agrees well with absorbance and micro-Raman characterization.

Device performance was evaluated by the peak transconductance $g_m = dI_{ds}/dV_g$, estimated to be approximately 1.8 μS at V_{ds} = 1 V, and the hole mobility, calculated based on a parallel plate capacitor model for our thin film SWCNT transistor:

$$\mu = \frac{L}{WC_g}\frac{1}{V_{ds}}\frac{dI_{ds}}{dV_g} \sim 1.5 \mathrm{cm}^2/\mathrm{V}\cdot\mathrm{s}$$

where L = 2 μm, W = 200 μm, and C_g is the gate capacitance per unit area. The relatively large on-state conductance reflects the high purity of our SWCNT sample.[38] Our mobility compares favorably with values reported by LeMieux *et al.*[1] for SWCNT films. We note that the mobility reported here should be a lower bound because of the non-uniform coverage of the SWCNT film between the electrodes and the contact resistance, which has been neglected in the calculation. More sophisticated fabrication methods should produce uniform and aligned SWCNTs that improve the device performance;[4,39,40] nonetheless, the devices presented here are of sufficient quality to demonstrate that the electrical properties of as-grown SWCNTs are significantly influenced by the catalyst composition.

The role of the catalyst particle in determining the chirality of nanotubes remains unresolved. Our findings show that a relationship exists between the catalyst composition and the nanotube chirality in terms of electronic type. Theoretical studies have proposed that during nanotube nucleation, the stability of the

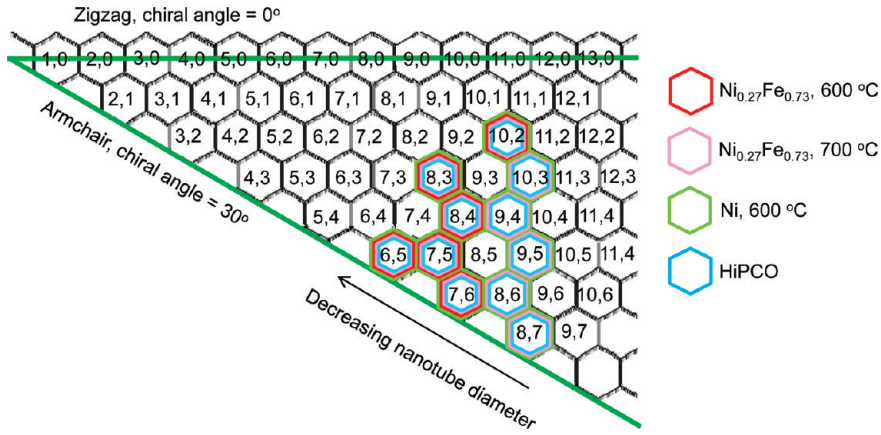

Figure 7. Summary of SWCNT chiralities detected by UV−visible−NIR absorbance spectroscopy in samples catalyzed by $Ni_{0.27}Fe_{0.73}$ at 600 and 700 °C and Ni at 600 °C. Results for HiPCO sample are also shown for reference.

cap, defined in terms of the energy associated with metal−carbon binding[24,41] and cap structure,[23] is controlled by the atomic-scale structure of the catalyst. Tuning the composition of Ni_xFe_{1-x} nanocatalysts results in subtle changes to the crystal structure, such as the transition from a fcc to bcc phase (Supporting Information, Table S1) that could influence the stability of certain caps and explain the selective growth of s-SWCNTs. Optical characterization indicates that SWCNTs prepared with $Ni_{0.27}Fe_{0.73}$ nanocatalysts contain higher concentrations of smaller diameter nanotubes than Ni nanocatalysts at 600 °C (Figure 7). In the small diameter limit, the formation of zigzag nanotubes has been proposed to be thermodynamically and kinetically unfavorable.[42] The remaining nanotubes in the small diameter range are semiconducting near-armchair and metallic armchair nanotubes. Recent reports suggest that the preference for near-armchair structures arises from a combination of cap stability and activation energy for carbon atom incorporation.[36,43] It is believed that the higher stability of armchair nanotube caps, as compared to near-armchair species, creates an activation barrier and results in decreased production of metallic nanotubes. Since the activated growth process is temperature-dependent, the selective growth of s-SWCNTs should no longer occur at higher temperatures, which is consistent with our experimental observations for $Ni_{0.27}Fe_{0.73}$-catalyzed SWCNTs at 700 °C (see Figure 2a).

In summary, we have demonstrated that engineering the composition of nanocatalysts at constant size permits selective growth of SWCNTs with uniform electronic properties. This approach was applied to the synthesis of $Ni_{0.27}Fe_{0.73}$ nanocatalysts, 2 nm in size, to produce highly enriched s-SWCNTs with a purity of close to 90% based on optical characterization and electrical studies in FET devices. The methodology presented here opens a route to designing catalysts for selective growth of semiconducting or metallic nanotubes of sufficient purity for direct integration in electronic applications.

METHODS

Sample Preparation. Metal nanoparticles were continuously synthesized in an atmospheric pressure microplasma reactor by nonthermal decomposition of nickelocene and ferrocene (Acros Inc., 99% purity). The relative concentrations of nickelocene and ferrocene in the vapor phase were controlled by varying the individual flow rates of the precursors. All gas flows were controlled by mass flow controllers that were carefully calibrated before experiments to precisely control the final metallocene concentration in the microreactor. The metallocene flow rate was varied with a balance of pure Ar gas to obtain final vapor concentrations between 1.2 and 3.0 ppm. The ratio of the Ni to Fe in the Ni_xFe_{1-x} bimetallic nanoparticles was estimated from the calculated vapor pressures of nickelocene and ferrocene in the reactor and is used to specify the Ni atom percent throughout this article (x = Ni atom %). The particle size and distribution were determined online by aerosol size classification using a cylindrical differential mobility analyzer (DMA) (TSI Inc., Model 3080N) and an ultrafine condensation particle counter (CPC) (TSI, Inc., Model 3076). In order to avoid Brownian coagulation of particles, size distributions of the metal particles were measured immediately downstream from the microplasma.

To catalyze CNT growth, the nanocatalysts synthesized in the microplasma reactor were directly introduced into a tubular flow furnace (Thermolyne, Model 20110) with 0.5 sccm C_2H_2 and 50 sccm H_2 and heated at 600 °C. The CNTs were nucleated and grown to a well-defined structure by controlling the catalyst diameter and composition, furnace temperature, and residence time in the tube furnace (1.8 cm i.d. × 30 cm length). Reactor product was collected downstream with a porous filter (Millipore Inc., glass fiber filter, 25 mm diameter) in the form of a black powder. Dispersions of CNTs were obtained by sonicating the collected material in 10 mL of 1 wt % sodium dodecyl sulfate (SDS)/D_2O (99.8 atom % D Acros Inc.) solution for 24 h. The upper 80−90% of supernatant was then carefully decanted, leaving micelle-suspended nanotube solutions. The dispersions were kept in an ice bath to avoid thermally induced changes to the chirality distribution.[44] Separation of individual SWCNTs was performed by centrifuging (Sorvall Instrument, model RC5B) for 2 h at 38 000g to remove the heavy multiwalled CNTs and bundled SWCNTs. The upper 80−90% of supernatant was then carefully decanted, leaving micelle-suspended nanotube solutions.

Catalyst Characterization. *Ex situ* microcharacterization of Ni, Fe, and NiFe nanoparticles synthesized in a microplasma was performed by HRTEM, EDX, and XRD. Thin films of materials were collected by directly depositing the aerosol particles leaving the microplasma reactor on carbon-coated copper TEM grids (Electron Microscopy Sciences, 200 mesh) or Si substrates with an electrostatic precipitator (TSI Inc., model 3089). HRTEM was performed using a Philips Tecnai F30 field emission high-resolution transmission electron microscope operated at 300 kV. To acquire the EDX spectrum from particle samples, the electron beam was focused on individual particles. XRD characterization was performed to determine the crystalline structure of the bimetallic nanoparticles with a Scintag X-1 advanced X-ray diffractometer using monochromated Cu Kα radiation (λ = 0.1542 nm).

SWCNT Characterization. UV−visible−NIR absorption spectra were collected on a Varian Cary 500 spectrophotometer. Spec-

tra were background-subtracted with a reference solution of 1% SDS/D_2O solution. The measurements were performed at room temperature in quartz cells with 10 mm path length. Additional assessment of the morphology of as-grown CNTs was attained by micro-Raman spectroscopy. Raman scattering studies were performed at room temperature with a Horiba Jobin Yvon LabRam HR800 spectrometer ($\lambda = 633$ nm) and an inVia Renishaw spectrometer ($\lambda = 488$ and 514.5 nm). Spectra were normalized by the G-band intensity and averaged from 10 random positions on each sample.

Device Fabrication and Electrical Characterization. SWCNTs dispersed in SDS/D_2O solutions were dropped onto 290 nm thick oxide/n-type Si substrate, which was used as a gate electrode. The substrate was kept at 50 °C to get rid of the water, rinsed gently with DI water, dried with nitrogen gas, and finally baked at about 190 °C to evaporate any water film remaining. Standard photolithography and electron beam evaporation of titanium/aluminum (1 nm/70 nm) were used to establish source and drain contacts. The photolithographically defined devices have typical width of $W = 200$ μm and length of $L = 2$ μm. After lift-off process, SWCNT thin film field-effect transistors (FETs) were characterized under ambient conditions at room temperature by measuring the drain current, I_{ds}, as a function of the source drain and gate voltages, V_{ds} and V_g, respectively.

Acknowledgment. The authors acknowledge the technical assistance of Amir Avishai (TEM), Alan K. McIlwain (XRD), Prof. Kenneth Singer (UV−visible−NIR), Regan Silvestri and Prof. Jack Koenig (micro-Raman spectroscopy), Prof. Mary Barkley and Prof. Eric Arts (ultracentrifuging), and Feng Du and Prof. Liming Dai at University of Dayton (multiline micro-Raman spectroscopy). X.G. thanks the ACS Petroleum Research Fund for partial financial support of the research. The authors are also grateful to Prof. C.C. Liu and Prof. John Angus for helpful discussions.

Supporting Information Available: Aerosol measurements, EDX characterization, XRD analysis, and UV−visible−NIR and micro-Raman spectroscopy. This material is available free of charge *via* the Internet at http://pubs.acs.org.

REFERENCES AND NOTES

1. LeMieux, M. C.; Roberts, M.; Barman, S.; Jin, Y. W.; Kim, J. M.; Bao, Z. N. Self-Sorted, Aligned Nanotube Networks for Thin-Film Transistors. *Science* **2008**, *321*, 101–104.
2. Javey, A.; Kim, H.; Brink, M.; Wang, Q.; Ural, A.; Guo, J.; McIntyre, P.; McEuen, P.; Lundstrom, M.; Dai, H. J. High-Kappa Dielectrics for Advanced Carbon-Nanotube Transistors and Logic Gates. *Nat. Mater.* **2002**, *1*, 241–246.
3. Bachtold, A.; Fuhrer, M. S.; Plyasunov, S.; Forero, M.; Anderson, E. H.; Zettl, A.; McEuen, P. L. Scanned Probe Microscopy of Electronic Transport in Carbon Nanotubes. *Phys. Rev. Lett.* **2000**, *84*, 6082–6085.
4. Kocabas, C.; Dunham, S.; Cao, Q.; Cimino, K.; Ho, X. N.; Kim, H. S.; Dawson, D.; Payne, J.; Stuenkel, M.; Zhang, H.; *et al.* High-Frequency Performance of Submicrometer Transistors That Use Aligned Arrays of Single-Walled Carbon Nanotubes. *Nano Lett.* **2009**, *9*, 1937–1943.
5. Baughman, R. H.; Zakhidov, A. A.; de Heer, W. A. Carbon Nanotubes—The Route Toward Applications. *Science* **2002**, *297*, 787–792.
6. *International Technology Roadmap for Semiconductors: Emerging Research Material*; ITRE Organization, 2007; pp 1−49 (http://www.itrs.net/).
7. Hersam, M. C. Progress Towards Monodisperse Single-Walled Carbon Nanotubes. *Nat. Nanotechnol.* **2008**, *3*, 387–394.
8. Krupke, R.; Hennrich, F.; von Lohneysen, H.; Kappes, M. M. Separation of Metallic from Semiconducting Single-Walled Carbon Nanotubes. *Science* **2003**, *301*, 344–347.
9. Chattopadhyay, D.; Galeska, L.; Papadimitrakopoulos, F. A Route for Bulk Separation of Semiconducting from Metallic Single-Wall Carbon Nanotubes. *J. Am. Chem. Soc.* **2003**, *125*, 3370–3375.
10. Arnold, M. S.; Green, A. A.; Hulvat, J. F.; Stupp, S. I.; Hersam, M. C. Sorting Carbon Nanotubes by Electronic Structure Using Density Differentiation. *Nat. Nanotechnol.* **2006**, *1*, 60–65.
11. Collins, P. C.; Arnold, M. S.; Avouris, Ph. Engineering Carbon Nanotubes and Nanotube Circuits Using Electrical Breakdown. *Science* **2001**, *292*, 706–709.
12. Zhang, G. Y.; Qi, P. F.; Wang, X. R.; Lu, Y. R.; Li, X. L.; Tu, R.; Bangsaruntip, S.; Mann, D.; Zhang, L.; Dai, H. J. Selective Etching of Metallic Carbon Nanotubes by Gas-Phase Reaction. *Science* **2006**, *314*, 974–977.
13. Zhang, L.; Zaric, S.; Tu, X. M.; Wang, X. R.; Zhao, W.; Dai, H. J. Assessment of Chemically Separated Carbon Nanotubes for Nanoelectronics. *J. Am. Chem. Soc.* **2008**, *130*, 2686–2691.
14. Qu, L. T.; Du, F.; Dai, L. M. Preferential Syntheses of Semiconducting Vertically Aligned Single-Walled Carbon Nanotubes for Direct Use in FETs. *Nano Lett.* **2008**, *8*, 2682–2687.
15. Li, Y. M.; Mann, D.; Rolandi, M.; Kim, W.; Ural, A.; Hung, S.; Javey, A.; Cao, J.; Wang, D. W.; Yenilmez, E.; *et al.* Preferential Growth of Semiconducting Single-Walled Carbon Nanotubes by a Plasma Enhanced CVD Method. *Nano Lett.* **2004**, *4*, 317–321.
16. Wang, B.; Wei, L.; Yao, L.; Li, L. J.; Yang, Y. H.; Chen, Y. Pressure-Induced Single-Walled Carbon Nanotube (*n*,*m*) Selectivity on Co-Mo Catalysts. *J. Phys. Chem. C* **2007**, *111*, 14612–14616.
17. Wang, B.; Poa, C. H. P.; Wei, L.; Li, L. J.; Yang, Y. H.; Chen, Y. (*n*,*m*) Selectivity of Single-Walled Carbon Nanotubes by Different Carbon Precursors on Co-Mo Catalysts. *J. Am. Chem. Soc.* **2007**, *129*, 9014–9019.
18. Ding, L.; Tselev, A.; Wang, J. Y.; Yuan, D. N.; Chu, H. B.; McNicholas, T. P.; Li, Y.; Liu, J. Selective Growth of Well-Aligned Semiconducting Single-Walled Carbon Nanotubes. *Nano Lett.* **2009**, *9*, 800–805.
19. Nikolaev, P.; Bronikowski, M. J.; Bradley, R. K.; Rohmund, F.; Colbert, D. T.; Smith, K. A.; Smalley, R. E. Gas-Phase Catalytic Growth of Single-Walled Carbon Nanotubes from Carbon Monoxide. *Chem. Phys. Lett.* **1999**, *313*, 91–97.
20. Liu, Q. F.; Ren, W. C.; Chen, Z. G.; Wang, D. W.; Liu, B. L.; Yu, B.; Li, F.; Cong, H. T.; Cheng, H. M. Diameter-Selective Growth of Single-Walled Carbon Nanotubes with High Quality by Floating Catalyst Method. *ACS Nano* **2008**, *2*, 1722–1728.
21. Cheng, H. M.; Li, F.; Su, G.; Pan, H. Y.; He, L. L.; Sun, X.; Dresselhaus, M. S. Large-Scale and Low-Cost Synthesis of Single-Walled Carbon Nanotubes by the Catalytic Pyrolysis of Hydrocarbons. *Appl. Phys. Lett.* **1998**, *72*, 3282–3284.
22. Bachilo, S. M.; Balzano, L.; Herrera, J. E.; Pompeo, F.; Resasco, D. E.; Weisman, R. B. Narrow (*n*,*m*)-Distribution of Single-Walled Carbon Nanotubes Grown Using a Solid Supported Catalyst. *J. Am. Chem. Soc.* **2003**, *125*, 11186–11187.
23. Reich, S.; Li, L.; Robertson, J. Control the Chirality of Carbon Nanotubes by Epitaxial Growth. *Chem. Phys. Lett.* **2006**, *421*, 469–472.
24. Ding, F.; Larsson, P.; Larsson, J. A.; Ahuja, R.; Duan, H. M.; Rosen, A.; Bolton, K. The Importance of Strong Carbon−Metal Adhesion for Catalytic Nucleation of Single-Walled Carbon Nanotubes. *Nano Lett.* **2008**, *8*, 463–468.
25. Chiang, W. H.; Sankaran, R. M. Linking Catalyst Composition to Chirality Distributions of As-Grown Single-Walled Carbon Nanotubes by Tuning Ni_xFe_{1-x} Nanoparticles. *Nat. Mater.* **2009**, *8*, 882–886.
26. Harutyunyan, A. R.; Chen, G. A.; Paronyan, T. M.; Pigos, E. M.; Kuznetsov, O. A.; Hewaparakrama, K.; Kim, S. M.; Zakharov, D.; Stach, E. A.; Sumanasekera, G. U. Preferential Growth of Single-Walled Carbon Nanotubes with Metallic Conductivity. *Science* **2009**, *326*, 116–120.
27. Chiang, W. H.; Sankaran, R. M. Microplasma Synthesis of Metal Nanoparticles for Gas-Phase Studies of Catalyzed Carbon Nanotube Growth. *Appl. Phys. Lett.* **2007**, *91*, 121503.

28. Chiang, W. H.; Sankaran, R. M. In Flight Dimensional Tuning of Metal Nanoparticles by Microplasma Synthesis for Selective Production of Diameter-Controlled Carbon Nanotubes. *J. Phys. Chem. C* **2008**, *112*, 17920–17925.
29. Chiang, W. H.; Sankaran, R. M. Synergistic Effects in Bimetallic Nanoparticles for Low Temperature Carbon Nanotube Growth. *Adv. Mater.* **2008**, *20*, 4857–4861.
30. McKeehan, L. W. The Crystal Structure of Iron−Nickel Alloys. *Phys. Rev.* **1923**, *21*, 402–407.
31. Hansen, M.; Anderko, K. *Constitution of Binary Alloys*; McGraw-Hill Book Company: New York, 1958; pp 677−684.
32. Strano, M. S.; Dyke, C. A.; Usrey, M. L.; Barone, P. W.; Allen, M. J.; Shan, H. W.; Kittrell, C.; Hauge, R. H.; Tour, J. M.; Smalley, R. E. Electronic Structure Control of Single-Walled Carbon Nanotube Functionalization. *Science* **2003**, *301*, 1519–1522.
33. Dresselhaus, M. S.; Dresselhaus, G.; Saito, R.; Jorio, A. Raman Spectroscopy of Carbon Nanotubes. *Phys. Rep.* **2005**, *409*, 47–99.
34. Bachilo, S. M.; Strano, M. S.; Kittrell, C.; Hauge, R. H.; Smalley, R. E.; Weisman, R. B. Structure-Assigned Optical Spectra of Single-Walled Carbon Nanotubes. *Science* **2002**, *298*, 2361–2366.
35. Kataura, H.; Kumazawa, Y.; Maniwa, Y.; Umezu, I.; Suzuki, S.; Ohtsuka, Y.; Achiba, Y. Optical Properties of Single-Wall Carbon Nanotubes. *Synth. Met.* **1999**, *103*, 2555–2558.
36. Naumov, A. V.; Kuznetsov, O. A.; Harutyunyan, A. R.; Green, A. A.; Hersam, M. C.; Resasco, D. E.; Nikolaev, P. N.; Weisman, R. B. Quantifying the Semiconducting Fraction in Single-Walled Carbon Nanotube Samples through Comparative Atomic Force and Photoluminescence Microscopies. *Nano Lett.* **2009**, *9*, 3203–3208.
37. Samsonidze, G. G.; Chou, S. G.; Santos, A. P.; Brar, V. W.; Dresselhaus, G.; Dresselhaus, M. S.; Selbst, A.; Swan, A. K.; Unlu, M. S.; Goldberg, B. B.; *et al.* Quantitative Evaluation of the Octadecylamine-Assisted Bulk Separation of Semiconducting and Metallic Single-Wall Carbon Nanotubes by Resonance Raman Spectroscopy. *Appl. Phys. Lett.* **2004**, *85*, 1006–1008.
38. Engel, M.; Small, J. P.; Steiner, M.; Freitag, M.; Green, A. A.; Hersam, M. C.; Avouris, Ph. Thin Film Nanotube Transistors Based on Self-Assembled, Aligned, Semiconducting Carbon Nanotube Arrays. *ACS Nano* **2008**, *2*, 2445–2452.
39. Cao, Q.; Rogers, J. A. Ultrathin Films of Single-Walled Carbon Nanotubes for Electronics and Sensors: A Review of Fundamental and Applied Aspects. *Adv. Mater.* **2009**, *21*, 29–53.
40. Kang, S. J.; Kocabas, C.; Ozel, T.; Shim, M.; Pimparkar, N.; Alam, M. A.; Rotkin, S. V.; Rogers, J. A. High-Performance Electronics Using Dense, Perfectly Aligned Arrays of Single-Walled Carbon Nanotubes. *Nat. Nanotechnol.* **2007**, *2*, 230–236.
41. Yazyev, O. V.; Pasquarello, A. Effect of Metal Elements in Catalytic Growth of Carbon Nanotubes. *Phys. Rev. Lett.* **2008**, *100*, 156102.
42. Gomez-Gualdron, D. A.; Balbuena, P. B. The Role of Cap Chirality in the Mechanism of Growth of Single-Wall Carbon Nanotubes. *Nanotechnology* **2008**, *19*, 485604.
43. Lolli, G.; Zhang, L. A.; Balzano, L.; Sakulchaicharoen, N.; Tan, Y. Q.; Resasco, D. E. Tailoring (*n*,*m*) Structure of Single-Walled Carbon Nanotubes by Modifying Reaction Conditions and the Nature of the Support of CoMo Catalysts. *J. Phys. Chem. B* **2006**, *110*, 2108–2115.
44. Heller, D. A.; Barone, P. W.; Strano, M. S. Sonication-Induced Changes in Chiral Distribution: A Complication in the Use of Single-Walled Carbon Nanotube Fluorescence for Determining Species Distribution. *Carbon* **2005**, *43*, 651–653.